

RICE UNIVERSITY

Interfacial Charge Transfer in Nanoscale Polymer Transistors

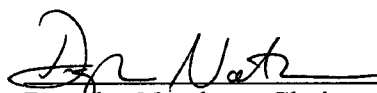
by

Jeffrey Howard Worne

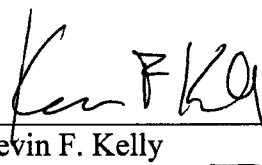
A THESIS SUBMITTED
IN PARTIAL FULFILLMENT OF THE
REQUIREMENTS FOR THE DEGREE

Master of Science

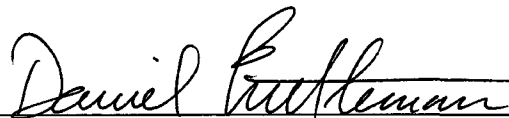
APPROVED, THESIS COMMITTEE:



Douglas Natelson, Chair
Associate Professor of Physics and
Astronomy and Electrical and Computer Engineering



Kevin F. Kelly
Associate Professor of Electrical and Computer
Engineering



Daniel M. Mittleman
Associate Professor of Electrical and Computer
Engineering

HOUSTON, TEXAS
MAY 2009

UMI Number: 1466856

INFORMATION TO USERS

The quality of this reproduction is dependent upon the quality of the copy submitted. Broken or indistinct print, colored or poor quality illustrations and photographs, print bleed-through, substandard margins, and improper alignment can adversely affect reproduction.

In the unlikely event that the author did not send a complete manuscript and there are missing pages, these will be noted. Also, if unauthorized copyright material had to be removed, a note will indicate the deletion.

UMI[®]

UMI Microform 1466856
Copyright 2009 by ProQuest LLC
All rights reserved. This microform edition is protected against
unauthorized copying under Title 17, United States Code.

ProQuest LLC
789 East Eisenhower Parkway
P.O. Box 1346
Ann Arbor, MI 48106-1346

ABSTRACT

Interfacial Charge Transfer in Nanoscale Polymer Transistors

by

Jeffrey Howard Worne

Interfacial charge transfer plays an essential role in establishing the relative alignment of the metal Fermi level and the energy bands of organic semiconductors. While the details remain elusive in many systems, this charge transfer has been inferred in a number of photoemission experiments. We present electronic transport measurements in very short channel ($L < 100$ nm) transistors made from poly(3-hexylthiophene) (P3HT). As channel length is reduced, the evolution of the contact resistance and the zero gate voltage conductance are consistent with such charge transfer. Short channel conduction in devices with Pt contacts is greatly enhanced compared to analogous devices with Au contacts, consistent with charge transfer expectations. Alternating current scanning tunneling microscopy (ACSTM) provides further evidence that holes are transferred from Pt into P3HT, while much less charge transfer takes place at the Au/P3HT interface.

Acknowledgments

I would like to thank the eternal patience and guidance afforded me by my advisor, Professor Douglas Natelson. Without his vision and interest in this project, it would have been difficult to make progress. Furthermore, his willingness to explain even the simplest of concepts and to answer some of the most banal of questions exemplifies the quality of his professorship. Thanks to Doug for giving me a deeper understanding of and appreciation for physics.

Also, thank you to my committee members, Kevin Kelly and Daniel Mittleman. I appreciate you taking time out of your busy schedules to listen to me drone on about my research.

A big thanks goes out to all the people in the Natelson lab, whose fruitful discussions and amusing anecdotes made coming to work everyday a little more bearable. Also, thanks to Angelo Benedetto and Tim Gilheart whose friendship have made my Rice experience much richer. Our daily hour of solace (lunch) is pretty good too.

Many thanks go out to my family, who have constantly encouraged me in all my activities. They believe I can do anything, and for that I will always be grateful.

Thank you to all the people I've met while at Rice (far too many to list), many of whom I consider close friends. I have grown to be a better person because I know you. As such, thank you to Valhalla. It's far more than just a bar - it's the spirit of graduate life. That dusty, dank, hole-in-the-wall has kept me sane and happy and brings together great people. VIVA VALHALLA!

Finally, thank you to Laura Jones. I have far too much to say about how awesome you are and how much I love you than can be contained in a simple acknowledgments page. Suffice it to say, though, that you're a douchebague. And there's nothing

you can do to respond because it's permanently here, in ink, bound for eternity. Ha.

fingers dancing

Contents

Abstract	ii
Acknowledgments	iii
List of Illustrations	vi
1 Introduction	1
1.1 Organic Semiconductors	1
1.2 Molecular Structure	3
1.3 Charge Transport	5
1.4 Metal/Organic (MO) Interface	6
1.5 Organic Field-Effect Transistors (OFETs)	10
1.6 Alternating Current Scanning Tunneling Microscopy	13
1.7 This Thesis	14
2 Interfacial Charge Transfer in Nanoscale Polymer Transistors	16
2.1 Introduction	16
2.2 Transmission Line Measurements	18
2.3 Device Fabrication	19
2.4 Results and Discussion	21
2.5 Conclusions	30
3 Final Remarks and Future Direction	32
Bibliography	34

Illustrations

- 1.1 Today's state-of-the-art full-color, flexible organic-based display made by Sony. 2
- 1.2 Regioregular P3HT (left), TIPS pentacene (middle), rubrene (right). The first two materials are widely studied in organic semiconductor research and show the most promise as high mobility, solution processable electronic materials. The third has exhibited some of the highest mobilities for any organic semiconductor. 4
- 1.3 Schottky-Mott and non-Schottky-Mott behavior. In (A), no contact exists between the metal and the OSC. The HOMO and LUMO levels are Gaussian in shape due to energetic disorder. The Schottky-Mott limit is shown in (B), with the traditional Schottky barrier shown as φ_{SM} . The work function of the OSC then becomes $\varphi_{sub/organic}$. Because there are no available states in the gap, no charge transfer occurs. In (C), charge transfer has occurred at the MO interface, creating an interfacial dipole, Δ , and Fermi level pinning. This is believed to occur once the Fermi level of the substrate is equal to the polaron formation energy, E_P , in the polymer. 8

- 1.4 (a) Bottom-contact FET. P3HT is spun coated onto the FET device to a thickness of 5nm. This causes the P3HT to lie below the top of the electrode. Current flows from one contact, across the P3HT layer and into the other contact. (b) Scanning electron micrograph of a 127nm gap fabricated using 2-step electron beam lithography. Electrode widths are $1\mu\text{m}$ 11
- 1.5 P3HT FET with Pt electrodes operated in the linear regime. P3HT is a well-behaved organic semiconductor. 13
- 2.1 Cartoon describing the transmission line approach, with traditional contact resistance extrapolation, and deviation expected if the MO interface does not behave like the bulk. This deviation should occur on the 100nm length scale. Inset: Actual transmission line measurements. Note the linear nature over several tens of microns. Film continuity is often assumed in our samples, and conduction even in the longest channels verifies our films are not broken over at least the $50\mu\text{m}$ scale. 18
- 2.2 Device resistance versus channel length for Au, Au/f-OPE and Pt electrodes. Note the upturn in resistance for short channel lengths in Au devices. Data taken at low V_{SD} ($< -250\text{mV}$), $V_g = -70\text{V}$ and $T = 300\text{K}$. Inset: Short channel data from 100nm to 250nm presented for clarity. 22
- 2.3 AFM height and phase scans of Au (A,C) and Pt (B,D) electrodes. Very little differs between these two electrode materials, suggesting morphology is not an explanation for the variation in transport measurements. 23

- 2.4 I_D - V_{SD} curves for various V_G . Pt at left, Au at right. Note the order of magnitude difference between the Pt and Au currents, as well as the non-zero two terminal conduction in the Pt case. Channel length is 144nm, channel width is $50\mu\text{m}$, $T = 300\text{K}$ for both devices. As the channel length increases, the ZGB differences diminish. 25
- 2.5 (a) $V_G = 0$, two-terminal current (ZGB) versus channel length for Au, Au/f-OPE and Pt devices (legend in figure 2.2). The ZGB current is nearly identical for the $5\mu\text{m}$ channel but rapidly diverges as the channel lengths decrease, with Pt electrodes showing a strong increase in current. Inset: detail of current measured in the shortest channels. (b) Pt devices fabricated using the method in [1]. ZGB data collected at $V_{SD} = -500\text{mV}$ 26
- 2.6 Topography (A,C) and ACSTM (B,D) of Au (A,B) and Pt(C,D) films with P3HT deposited on top. All images were acquired at -1.0V sample bias, 10pA tunneling current and are $473\text{nm} \times 473\text{nm}$. The scale bars in all images are 94.6nm . The color bars are in units of nm for the topography images and in mV for the ACSTM images. The greater magnitude in (D) indicates a greater population of holes than in (B). 28

Chapter 1

Introduction

1.1 Organic Semiconductors

Devices based on organic semiconductors (OSC) have recently become a viable replacement for silicon-based electronics in a variety of applications. Recent implementations have centered on display technologies, such as flexible screens and ultra-thin displays. An illustrative device of this type is shown in figure 1.1[2]. Future implementations of organic electronics center on inexpensive consumer devices used in places where conventional silicon-based devices cannot be used, either because of cost or physical limitations. Disposable electronics, color electronic paper, and smart clothing with embedded OSC devices have all been proposed as potential applications for this class of material. However, because of their significantly lower mobilities they will not replace silicon as the material of choice for high-speed electronic devices. Mobility is a metric used to characterize the freedom of charge carriers to move throughout a semiconductor, and will be covered in more detail in section 1.3.

Organic semiconductors are not new, being first discovered in the early 20th century [3] with the development of anthracene crystals. These crystals, while semiconducting, had poor stability and very low mobilities. Advances in material science and chemical engineering have since created a wealth of organic semiconductors [4] capable of both hole- and electron-transport. Consequently, organic LEDs, organic solar cells and organic field-effect transistors are all becoming viable technologies.

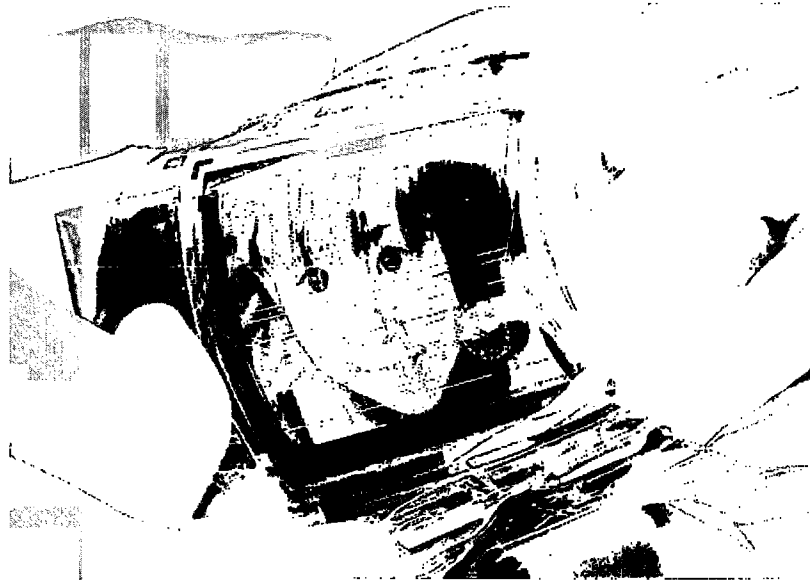


Figure 1.1 : Today's state-of-the-art full-color, flexible organic-based display made by Sony.

Besides OLED displays, organic electronic materials are becoming commonplace in applications that require low power but are also easily read in bright light. Recently, Esquire magazine published a commemorative 75th anniversary issue using electronic ink for a portion of their cover [5]. While the display itself is not made from OSCs, the potential to use them as the drive electronics for the display is high. This would allow for an ultra-thin, flexible device, capable of being folded up like a conventional newspaper. As the desire for thinner, lower power, simple and low-cost processing increases, organic materials become more attractive. As such, the need for an accurate understanding of the physical principles behind organic materials becomes paramount, and will help shape future technologies.

1.2 Molecular Structure

Organic semiconductors, on the simplest level, behave like their inorganic counterparts, and are often used as LEDs, diodes and transistors. Typical band gaps for organic materials lie between 1.5 and 3 eV [3], and because they are direct band gap materials, this makes them an excellent for both optical absorption and emission in the visible range. Recent advancements in organic photovoltaic devices exploit this fact in order to make inexpensive solar cells, and organic LEDs displays have richer, brighter colors than traditional silicon-based displays.

While the superficial behavior of organic and inorganic semiconductors appears similar, the physics behind this behavior are very different. The conduction and valence bands in inorganic semiconductors arise from the crystalline nature of the semiconductor lattice. The periodicity of the lattice structure prohibits certain energies of electrons from propagating through the crystal while allowing delocalized electronic states of other energies. This is the origin of conduction and valence bands, and the energy gap between them. For a complete treatment on inorganic semiconductors, see ref. [6]. Organic materials have conduction and valence bands as well, built up from the hybridization of the lowest unoccupied molecular orbital (LUMO) and highest occupied molecular orbital (HOMO). Unlike inorganic semiconductors, OSCs develop their transport characteristics via pi-electron delocalization, thereby allowing charge carriers to move along and between the molecular backbones. The HOMO and LUMO levels are molecule specific and do not necessarily arise from long range ordering as in the inorganic semiconductor case. Additional information on charge carrier transport will be covered in a later section.

Conjugated molecules used as organic semiconductors are typically either a rigid, single crystal or a flexible, disordered network of interacting molecules. The single

crystalline organic materials are grown via vapor phase deposition, and crystals grown from rubrene molecules have shown mobilities of $20 \text{ cm}^2/\text{Vs}$ [7]. This is roughly a factor of 100 improvement in mobility over typical organic materials, and is owed to the long-range ordering within the grown crystal and very low defect density. Crystals grown in this way behave more like inorganic semiconductors. On the other end of the spectrum lie organic molecules commonly deposited from solution. The mobility of these structures is typically less than $1 \text{ cm}^2/\text{Vs}$, and is largely due to the disordered network of molecules throughout the conducting region. For efficient charge transfer to occur, the electronic pi-orbitals should overlap between neighboring molecules [8]; the disorder, however, prevents easy charge transfer between molecular backbones because the pi-orbitals cannot easily align. While some evidence points to crystalline ordering of the molecules on the nanoscale [9], mobilities approaching that of the single-crystal organic semiconductors have yet to be measured. Three common organic semiconductors are pictured in figure 1.2, regioregular poly(3-hexylthiophene) (P3HT) [10], TIPS-pentacene [11] and rubrene [12].

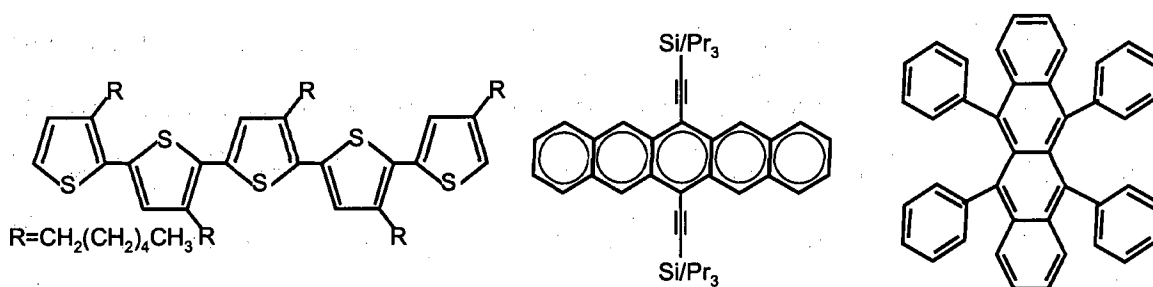


Figure 1.2: Regioregular P3HT (left), TIPS pentacene (middle), rubrene (right). The first two materials are widely studied in organic semiconductor research and show the most promise as high mobility, solution processable electronic materials. The third has exhibited some of the highest mobilities for any organic semiconductor.

The organic semiconductor used throughout this thesis is poly(3-hexylthiophene),

or P3HT. P3HT consists of a thiophene backbone, with alternating orientations of the thiophene groups giving head-to-tail (shown in figure 1.2) or head-to-head configurations. Tail-to-tail and tail-to-head configurations are also possible, but are not typically used. When this orderly combination of the thiophenes is present throughout, the P3HT is termed regioregular. Regioregularity improves mobility in deposited films as it better aligns the interchain pi-pi orbitals, which enhances charge transport between molecular chains as previously mentioned [8]. The hexyl side chains, shown as R in figure 1.2, are present to improve the solubility of P3HT into various solvents such as toluene, chloroform and dichlorobenzene.

1.3 Charge Transport

Understanding the nature of charge carrier transport in organic materials has been an area of active research for over two decades [13], and is an area that has high impact in the quality of future devices made with organic materials. This thesis does not deal with charge carrier transport, so only a brief discussion will follow. For a more complete treatment, see ref. [4].

An important metric used to describe semiconductors is mobility. Mobility is given by

$$\mu = v_d/E. \quad (1.1)$$

In this equation, v_d is the drift velocity of the charge carriers and E is the applied electric field. Thus, under a fixed applied electric field, charge carriers that have a higher drift velocity will have a higher mobility, implying a reduced impedance to charge carrier motion. Typical values for mobility in OSCs are around $0.1 \text{ cm}^2/\text{Vs}$ [14] whereas silicon can have mobilities greater than $1000 \text{ cm}^2/\text{Vs}$ [6].

Mobility, therefore, influences charge transport in organic materials and is strongly

dependent on the ordering found in the deposited film [3]. For highly purified, ordered molecular crystals, transport can be considered band-like, with a power law temperature dependence on the mobility of the form

$$\mu \propto T^{-n} \quad n = 1 \dots 3. \quad (1.2)$$

This behavior of mobility to temperature is indicative of band transport [3]. In general, however, disorder in the film eliminates any long-range ordering, and charge transport is generally viewed as variable range hopping (VRH) [4]. In this view, charge carriers move throughout the polymer film by thermally assisted hopping events from one molecular chain to another. The mobility of these systems is of the form

$$\mu \propto \exp \frac{E_A}{k_B T}, \quad (1.3)$$

where E_A is the activation energy required to hop between chains [3]. As such, mobilities in disordered organic polymers are highly temperature dependent. Previous work [15, 16] done on transport and injection into P3HT has shown data consistent with hopping transport and injection into a disordered density of localized states.

1.4 Metal/Organic (MO) Interface

In addition to having a thorough understanding of charge transport in organic materials, the nature of the interface between organic materials and metal electrodes remains important for both basic physical research and technological applications [17]. Because contact with macroscopic devices must eventually be made, engineering an optimal interface between metals and OSCs will enhance device performance. Additionally, a basic physical understanding of the nature of metal/disordered polymer interactions will help us better understand similar systems and allow us to make predictions about new ones.

Any contamination on the surface of the metal will prevent direct contact of the OSC. Recent studies have found that using a self-assembled monolayer (SAM) on the metal electrode can have a profound impact on charge carrier injection into the polymer [18, 19, 20]. The relative ease at engineering the behavior between metals and organic polymers highlights the need for a more complete understanding of the nature of this interface. Tuning both the local chemistry and metal work function (Fermi level) give such physical insight.

As the metal work function changes, the OSC is forced to adapt energetically. Initially, the Schottky-Mott model was used to explain the interaction between the metal and the OSC, but was found that energy band alignment at the MO interface differs significantly from this expected behavior [21, 22]. In the Schottky-Mott model, the vacuum levels of the metal and semiconductor are aligned. Because the chemical potentials between the metal and semiconductor need to be equilibrated, charge transfer occurs and the energy levels in the semiconductor are altered to accommodate for this transfer; this is commonly known as band bending. Once equilibrium is established, a permanent energy barrier exists between the metal and semiconductor in the form of an electric field. This field is established when the charge carriers leave the semiconductor, leaving their ionized donor atoms behind. The height of the barrier is then, simply, the difference between the metal work function and the electron affinity of the semiconductor [6].

Unlike the relatively simple, idealized case of the metal/inorganic semiconductor interface, the MO interface is comparably more complicated. Both the theoretical treatment and the experimental analysis for this system have proven to be challenging [23]. Ultraviolet photoemission spectroscopy (UPS) and x-ray photoemission spectroscopy (XPS) are uniquely suited for investigating buried interfaces such as the MO

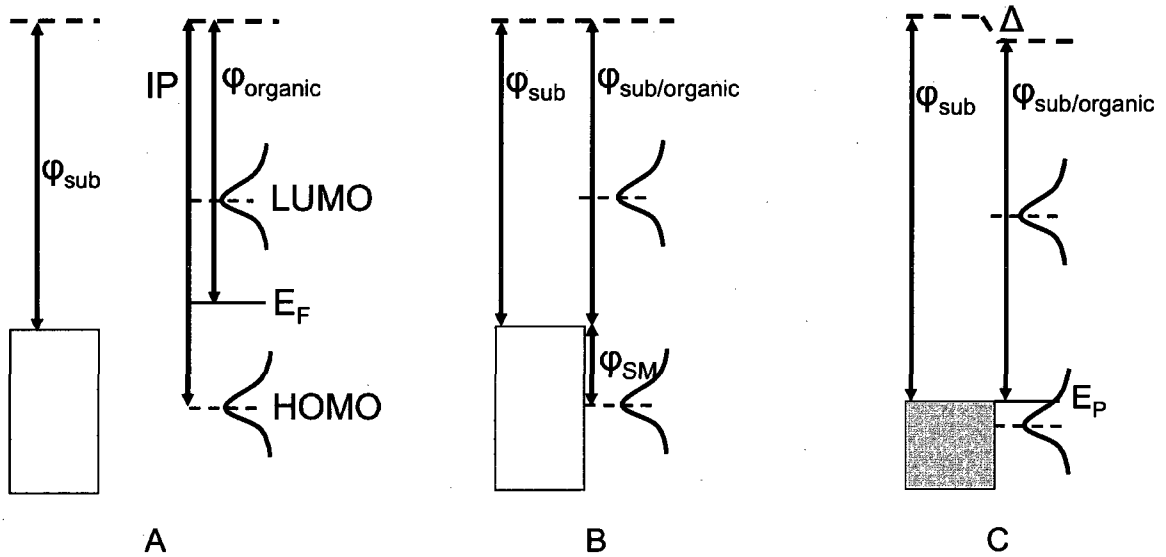


Figure 1.3 : Schottky-Mott and non-Schottky-Mott behavior. In (A), no contact exists between the metal and the OSC. The HOMO and LUMO levels are Gaussian in shape due to energetic disorder. The Schottky-Mott limit is shown in (B), with the traditional Schottky barrier shown as ϕ_{SM} . The work function of the OSC then becomes $\phi_{sub/organic}$. Because there are no available states in the gap, no charge transfer occurs. In (C), charge transfer has occurred at the MO interface, creating an interfacial dipole, Δ , and Fermi level pinning. This is believed to occur once the Fermi level of the substrate is equal to the polaron formation energy, E_P , in the polymer.

interface and have shown the error in assuming vacuum level alignment when these materials come into contact [21, 24]. Additionally, UPS and XPS experiments are able to view the change in important parameters at the MO interface - such as the work function of the metal, the ionization potential of the organic, the work function of the organic semiconductor and any interfacial energy barriers - as a function of organic material thickness.

In both MO [21] interfaces and organic/organic [24] interfaces, the work function of the substrate plays a pivotal role in how the system will equilibrate. Recent work [22, 25, 26, 27] has cataloged a wide-range of substrate/organic pairings and investigated the interfaces using UPS, illustrating two different regimes of MO interaction. For hole

injection, if the Fermi level of the substrate is less than a certain energy level, currently thought to be the positive polaron formation energy level, traditional Schottky-Mott vacuum level alignment will occur with no charge transfer [25], shown in figure 1.3(b). For electron injection, the Schottky-Mott picture occurs if the Fermi level is greater than the negative polaron formation energy level. In this regime, the work function of the organic material - defined as the difference between the Schottky barrier (φ_{SM}) and the ionization potential (IP) - will follow the work function of the substrate. An important parameter used to classify the MO interface is the slope parameter S , defined to be $S = d\varphi_{organic,sub}/d\varphi_{sub}$ where $\varphi_{organic,sub}$ is the work function of the organic material after being deposited onto the substrate and φ_{sub} is the work function of the substrate. For the Schottky-Mott limit, $S = 1$.

As the work function of the substrate is increased (decreased) for hole (electron) injection and becomes energetically equal to or larger than the polaron formation energy, charge transfer occurs at the MO interface. This causes the Fermi level of the organic material to be pinned at this energy level, preventing vacuum level alignment, illustrated in figure 1.3(c). In addition, an interfacial dipole is established which is manifest by a shift in energy of the HOMO and high-energy cutoff in the UPS spectra. This behavior suggests that the density of states available for charge transfer are highly localized at or near the polaron formation energy and exist nowhere else in the energy bandgap [25, 26]. Additionally, the S parameter becomes equal to zero, indicating that as the work function of the substrate increases further, no change in the interfacial dipole is measured. In this case, the work function of the OSC becomes equal to the polaron formation energy. In other words, using a higher (lower) work function substrate does not continue to improve the hole (electron) injection barrier, and a barrier to injection will always exist regardless of the substrate used.

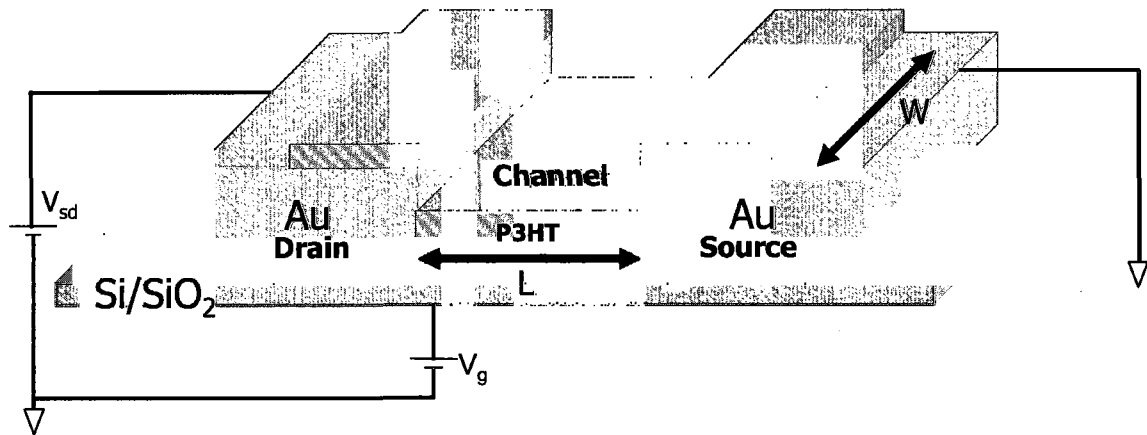
Experimental evidence of this charge transfer has been hard to obtain because of the nature of this buried interface. Recent experiments using electric force microscopy [28, 29] have directly measured the electric field at the interface and across the entire channel from source to drain. Transport measurements involving nanometer-scale channel length source-drain electrodes with a variety of work functions have not been performed, however. The length scale of charge transfer has certain boundaries placed on it, and is somewhere between 400nm - based on the resolution of scanning potentiometry experiments - and 10nm - where the electric field across this region would cause sample degradation, which does not occur [15]. Therefore, probing the region between these two extremes should be a direct measure of charge transfer at the MO interface.

By making electrical measurements across these electrodes, one can observe the effect of metal work function on electrical transport. This, coupled with existing UPS data, can help to give a more complete picture of the MO interface.

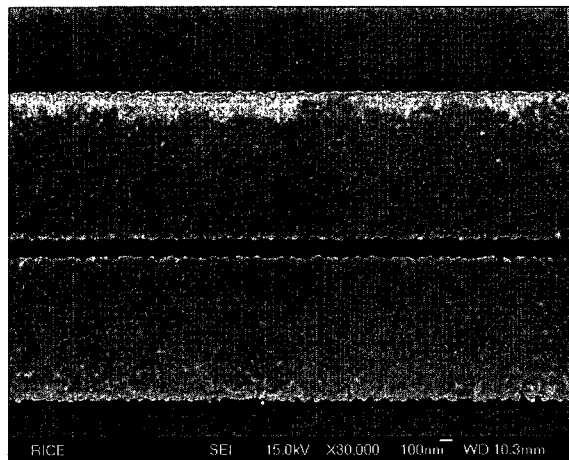
1.5 Organic Field-Effect Transistors (OFETs)

Several structures are used to investigate the properties of organic materials, namely the light-emitting diode, the bottom-contact field-effect transistor (FET) and the top-contact FET [3]. The FETs used have the advantage of a third contact, the gate, that allows for the modulation of charge carriers in the channel to increase or decrease the conductivity of the channel. Figure 1.4(a) shows a simple model of a bottom-contact FET.

Top-contact FETs are typically used for situations that require higher mobility and current densities. This is achieved because the area contacting the organic material is larger. Injection from the metal into the organic semiconductor can then occur



(a)



(b)

Figure 1.4 : (a) Bottom-contact FET. P3HT is spun coated onto the FET device to a thickness of 5nm. This causes the P3HT to lie below the top of the electrode. Current flows from one contact, across the P3HT layer and into the other contact. (b) Scanning electron micrograph of a 127nm gap fabricated using 2-step electron beam lithography. Electrode widths are 1μm.

along the entire length of the bottom of the contact. The drawback to this style of FET is the potential for damage to the semiconductor. The electrodes are typically thermally evaporated, and the high temperatures used in this type of evaporation can cause chemical changes in the organic material, as well as diffusion of the metal contact into the semiconductor. This is undesirable as it can affect injection data and make transport results difficult to interpret.

Bottom-contact FETs have a reduced area of contact to the organic semiconductor, but the semiconductor is not damaged during the fabrication stage. A more controlled environment is created, allowing for careful measurements of metal/organic interactions. Because a smaller area of the deposited organic material is contacted by the metal electrodes, measured mobilities and contact resistances are usually worse than top-contact FETs.

In FET devices, charge is injected via the source and drain electrodes, which are usually defined arbitrarily based on the voltage applied at each contact. In general, for the organic FETs in this thesis, the drain electrode has an applied bias whereas the source electrode is grounded. The source and drain electrodes also define the 'channel', which has dimensions of length and width, as shown in figure 1.4(a). The third contact in FET devices is the gate. The gate is typically degenerately doped silicon (n or p type) and is covered by an insulator, usually silicon dioxide (SiO_2). With the organic material on top, the gate acts as a parallel plate capacitor, and by modulating the gate voltage, one can attract more charge carriers into the channel thereby changing the conductivity of the semiconductor. FETs in our experiments are operated in the linear regime in order to remove any saturation effects. Additionally, we employ the transmission line technique (covered in section 2.2) in order to measure mobility and contact resistance, and this requires that the I-V data be linear as shown

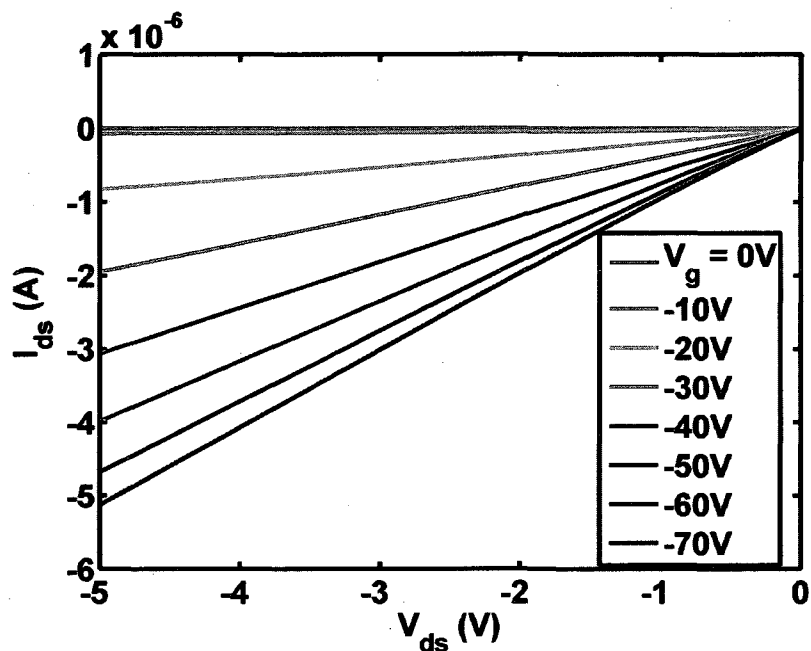


Figure 1.5 : P3HT FET with Pt electrodes operated in the linear regime. P3HT is a well-behaved organic semiconductor.

in figure 1.5.

1.6 Alternating Current Scanning Tunneling Microscopy

Alternating current scanning tunneling microscopy (ACSTM) is a technique originally used to characterize dopant profiles in inorganic semiconductors [30], but has since found uses outside the inorganic semiconductor community. In our work, the ACSTM was used in difference frequency mode, where the non-linear nature of the tunneling gap between the STM tip and sample are used to mix two microwave signals, f_1 and f_2 [31]. The second signal, f_2 , is slightly detuned from the first by Δf , usually several kHz. The mixing in the tunneling gap creates a signal at both the sum and difference frequencies. In this technique, a conventional lock-in amplifier is used to record the signal at Δf .

Dopant profiling is traditionally done using traditional capacitance-voltage measurements. In C-V measurements, one can determine the type of dopant and its rough concentration by sweeping a voltage and measuring the capacitance of a semiconducting structure. In the STM, however, one typically measures the tunneling current, not the capacitance of the tip/sample system; by using ACSTM, one can directly measure the C-V data. A simple model is presented in [30]. The tip and sample can be modeled as a parallel R-C network with R being the tunneling resistance and C arising from the sample. For an applied voltage $V_t = V_{dc} + v$, where v is the amplitude applied microwave signal, the measured current $I = V_t/(R||C)$. Since the microwave signal is the one of interest, the current equation reduces to

$$i = [1/R(V_t) + j\omega C(V_t)]v \quad (1.4)$$

which is the current measured from the input microwave signal. Since the dominant feature of interest is the capacitance of the system, the resistive term is ignored and equation 1.4 is expanded for small signals about V_{dc} , giving

$$i = j\omega[C(V)v e^{j(2\pi\Delta f)t} + C'(V)v^2 e^{2j(2\pi\Delta f)t} + C''(V)v^3 e^{3j(2\pi\Delta f)t} + \dots]. \quad (1.5)$$

Therefore, by measuring the second and third harmonics of the microwave signals at the difference frequency, one can get a differential C-V measurement. The dC/dV signal is then proportional to carrier density and carrier type in the semiconductor.

1.7 This Thesis

The main focus of this thesis is to discuss the metal contact/organic semiconductor interface and investigate the interaction between these types of materials. By varying the work function of the metal contact, we measure a significant difference in charge

mobility within and charge injection into the organic material. Our work is unique in that it uses devices with very short channels (in the tens of nanometer range) and high aspect ratio with metals of different work functions. This allows us a wide range of tools to investigate the nature of charge transfer at the MO interface.

In addition, we use ACSTM in order to qualitatively compare the MO interface with different substrates. We discover that substrates with higher work functions effectively dope the OSC with charge carriers, while substrates with lower work functions effectively deplete the polymer (or, at the very least, no charge is transferred). We also consider a morphological explanation to our transport data, but conclude that this does not adequately explain our results.

Chapter 2

Interfacial Charge Transfer in Nanoscale Polymer Transistors

2.1 Introduction

As discussed in the previous chapter, prior to this work the detailed behavior of the metal-organic (MO) interface had not been studied with transport measurements on the length scale of interfacial charge transfer (on the order of tens of nanometers). Several studies have been performed using ultraviolet spectroscopy (UPS) [25, 27] which have investigated the energy levels of the MO interface as an organic semiconductor (OSC) is deposited. They find evidence of Fermi level pinning and charge transfer for metals with work functions higher than the highest occupied molecular orbital (HOMO) in the polymer. For work functions lower than the HOMO level, traditional Schottky-Mott behavior is observed along with no charge transfer. Several explanations for this abrupt charge transfer have been presented; among them, the ‘pillow effect’ which reduces the length of the metal electron tail and causes a change in the interfacial dipole at the MO interface [32], formation of an induced density of states providing additional routes of charge transfer [33], and charge transfer involving the creation of polarons or bipolarons [25, 26].

While the UPS data show clear evidence of interfacial dipole formation and Fermi level pinning, transport data that directly probes the region of charge transfer has not yet been performed for high performance OSCs such as P3HT. Transport measure-

ments involving contact resistance measurements [20, 34] have shown large variations in contact resistance based on electrode material, with higher work function materials remaining ohmic even after several hours of dedoping. These results are consistent with the idea that high work function metals effectively dope the OSC near the interface. Additionally, by scaling the channel length L down but keeping the channel width fixed, channel mobility increases and overall channel resistance decreases. Previous work [14, 15] has simply extrapolated this trend to zero channel length and taken the $L = 0$ value to be an estimate of contact resistance. If charge transfer does occur, however, this *a priori* extrapolation is not accurate. This is covered further in section 2.2.

In order to investigate these ideas experimentally, we fabricated metal electrodes with channel lengths, L , ranging from 50nm to 5 μ m. With platinum electrodes, we notice a drop in resistance as L reaches 100nm. Additionally, this decrease in resistance corresponds to a 10-fold increase in zero gate bias (ZGB) current. In identically prepared gold electrodes, we notice an increase in resistance as L approaches 100nm and measure ZGB currents an order of magnitude lower than those measured with Pt electrodes. Au electrodes were also treated with a self-assembling monolayer (SAM), used previously [20] to increase the work function of gold, with results intermediate to the Pt and bare Au cases. As additional evidence for interfacial charge transfer, AC-STM was performed on identically prepared films of P3HT on Au and Pt substrates. Data from the Pt substrate shows strong evidence for hole transfer into P3HT, in contrast to very little transfer into P3HT on the Au substrate.

2.2 Transmission Line Measurements

In previous work performed in our group [14, 15, 20, 34], the transmission line technique was used to characterize the contact resistance and bulk mobility of the P3HT films. Drain current, I_D , versus source-drain bias, V_{SD} , data sweeps were collected for various gate voltages, V_G , in the shallow channel regime ($V_{SD} \ll V_G$). This ensured our I-V sweeps were linear, removing any channel saturation effects. In the transmission line approach, $(dI_D/dV_{SD})^{-1}$ is plotted versus L for a particular gate voltage. An example of this technique is shown in figure 2.1. The slope of this line is the channel resistance, and the extrapolated y-intercept of the line is taken to be the contact resistance.

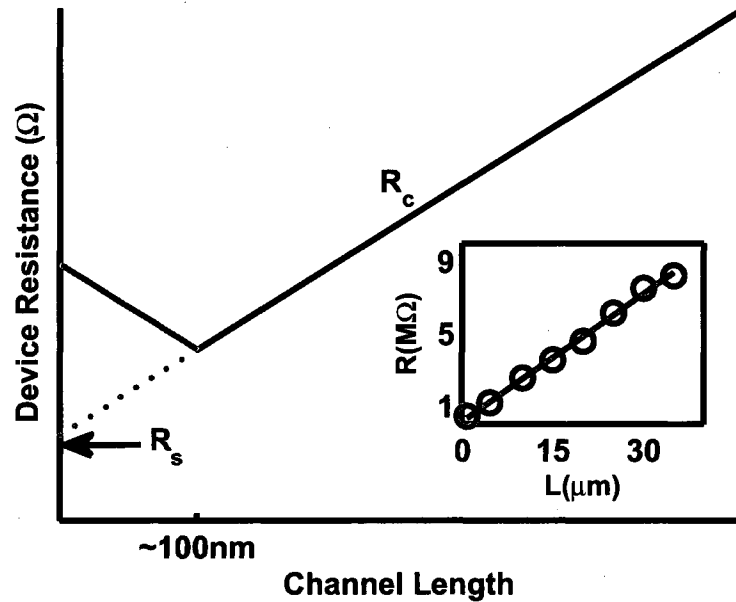


Figure 2.1 : Cartoon describing the transmission line approach, with traditional contact resistance extrapolation, and deviation expected if the MO interface does not behave like the bulk. This deviation should occur on the 100nm length scale. Inset: Actual transmission line measurements. Note the linear nature over several tens of microns. Film continuity is often assumed in our samples, and conduction even in the longest channels verifies our films are not broken over at least the $50\mu\text{m}$ scale.

This extrapolation assumes the behavior of the P3HT is uniform down to arbitrarily short length scales. However, film morphology near the contacts may not be as uniform as the bulk, and can lead to deviations from the linearity found in $R(L)$ [35]. Additionally, as previously mentioned, depletion effects based on charge transfer from the polymer into the electrodes could leave an area of poor conduction behind. These areas would need to be between 10nm-400nm away from each electrode, based on current physical understanding and resolution limits of scanning potentiometry experiments. This effective depletion region would lead to an upturn in measured device resistance as these two areas overlapped. The effect of these non-idealities is illustrated by the red upturned line in figure 2.1.

2.3 Device Fabrication

Samples were prepared on degenerately doped n^+ silicon wafers with 200nm of thermally grown oxide. The wafers were cleaned in acetone and isopropanol before being cleaned in oxygen plasma. Electrodes were then patterned using standard electron beam lithography. Channel lengths from 50nm to $5\mu\text{m}$ with widths fixed at $50\mu\text{m}$ were created using two-step lithography. Additionally, long channel devices with interdigitated electrodes (L ranging from $1\mu\text{m}$ to $50\mu\text{m}$, W fixed at $200\mu\text{m}$) were included on the same chip in order to measure bulk film mobility and contact resistances using the transmission line technique. Pt and Au films were deposited via a 10kW electron beam evaporator to a thickness of 15nm, with a 1nm Ti adhesion layer. Following lift-off in acetone, the fabricated structures were cleaned in oxygen plasma for 2 minutes, followed by a submission into piranha solution (3:1 H_2SO_4 :30% H_2O_2) for 90 seconds. For some Au electrodes, fluorinated oligo(phenylene ethynylene) (f-OPE) at a concentration of 0.25mg/mL was dissolved in a 1:1 mixture of ethanol and

chloroform under nitrogen gas and allowed to assemble on the Au electrode surface for 24 hours to increase the work function of the electrodes. Standard thioacetate chemistry was used in order to deprotect the f-OPE and allow it to assemble onto the Au surface [36].

For electrodes smaller than 50nm, we used a self-aligning technique involving sacrificial Cr layers evaporated on top of the desired Pt or Au structures [1]. During our second lithography step, rectangular windows were created above the Ti/Au or Pt/Cr structure using electron beam lithography and additional Au or Pt was deposited. The Cr oxide acts as a shadow mask, with an oxide overlap of a few (<10) nanometers. This creates devices with a very high aspect ratio and channel length of 15nm. These high aspect ratio devices will be discussed later, showing the extreme limit of charge transfer transport measurements.

Prior to depositing the P3HT, the final structures were treated with $8\mu\text{L}$ of octadecyltrichlorosilane (OTS) in 8mL of hexadecane, in the dark for 12-24 hours. The OTS serves as an oxide passivation layer, removing traps at the OSC/insulator interface and improving mobility. P3HT, 0.1% by wt. in high purity chloroform is then spun coat to a final thickness of 5nm (as verified by atomic force microscopy (AFM)). Contact is made to the silicon wafer through the oxide, which becomes the gate electrode.

For samples used in ACSTM, Au and Pt films were evaporated and cleaned using the above procedures. No SAMs were applied to either surface. P3HT was then spun onto these surfaces and the samples were taken for analysis.

All transport experiments were performed using a Hewlett-Packard 4145B in a Desert Cryogenics probe station with a base pressure of 1×10^{-6} torr. Ambient light was blocked from entering the probe station to avoid photoexcitation of the P3HT.

Samples were also pumped on for at least one hour before measurements were performed in order to remove any stray dopants. In order to isolate the electrodes from the gate (as the P3HT film was continuous and would short to the gate), a probe tip was dragged in a rectangular window as an outline of each electrode, isolating them from the gate as well as from each other.

2.4 Results and Discussion

Transport data from our 50nm-5 μ m structures was collected for Au, Pt and Au treated with f-OPE. All data was taken with a V_{SD} voltage sweep from 0V to -500mV, and V_G sweep from 0V to -70V in -10V steps. From our I-V curves, we generated an R versus L plot, shown in figure 2.2. Based on the transmission line calculations on our longer channel devices, the measured mobilities taken at $V_G = -70V$ were 5.3×10^{-2} cm²/Vs for Au, 5.3×10^{-2} cm²/Vs for Au/f-OPE, and 8.7×10^{-2} cm²/Vs for Pt.

Several differences stand out immediately upon inspection of the figure. The longest channel lengths (5 μ m) span nearly an order of magnitude in resistance, with the Pt devices lowest. As the channel lengths decrease, this gap grows until they span nearly two orders of magnitude. The Au devices start to show a general upturn in device resistance as the channel length decreases, while the Pt devices trend downward in device resistance. The f-OPE treated Au electrodes are intermediate in device resistance.

We note that the very short channel devices (as shown in the inset of figure 2.2) do not monotonically increase with decreasing channel length. Additionally, we notice large device-to-device variability among samples. This variability between devices on a single chip is likely due to variations in contamination at the MO interface. The

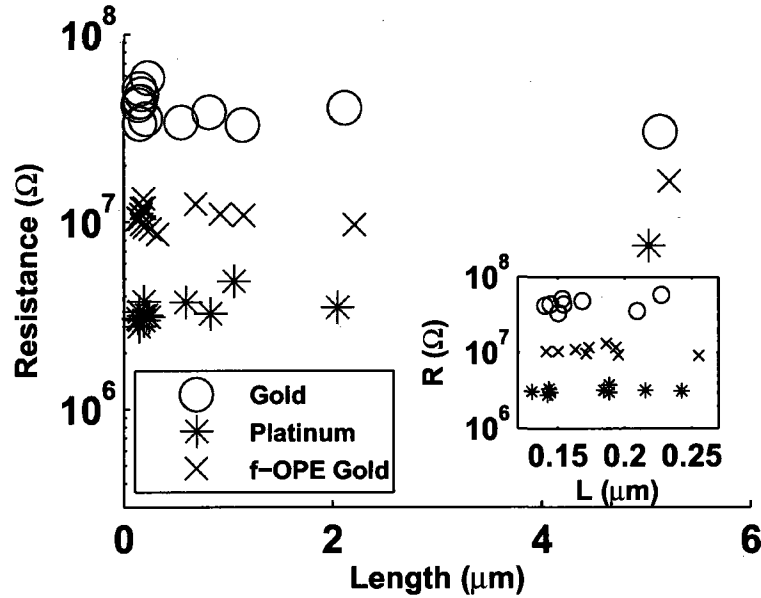


Figure 2.2 : Device resistance versus channel length for Au, Au/f-OPE and Pt electrodes. Note the upturn in resistance for short channel lengths in Au devices. Data taken at low V_{SD} ($< -250\text{mV}$), $V_g = -70\text{V}$ and $T = 300\text{K}$. Inset: Short channel data from 100nm to 250nm presented for clarity.

two step lithography process is prone to introducing additional chemical contamination, and thorough cleaning is difficult while maintaining the integrity of fabricated devices. Nevertheless, the overall trends and qualitative differences between electrode materials are clear.

Our first attempt at explaining the differences between Au and Pt substrates was that the films had different morphologies near these electrode materials. In order to investigate this question, we took $3\mu\text{m} \times 3\mu\text{m}$ atomic force microscopy (AFM) scans of the area near both Pt and Au electrodes. Height and phase data were collected, shown in figure 2.3. For the height data, the RMS roughness was 0.83nm for the area near the Au electrodes on the silicon oxide and 0.78nm near the Pt electrodes on the oxide. The two films, prepared identically, appear to have similar topological

characteristics. The phase data shows the films in more detail, namely the fibril nature of our deposited P3HT. Upon close inspection, however, very little difference between the two phase images can be seen. Down to the resolution of the AFM, little morphological difference is observable. The AFM data suggests that morphology is not an explanation to the deviations seen in our electrical measurements.

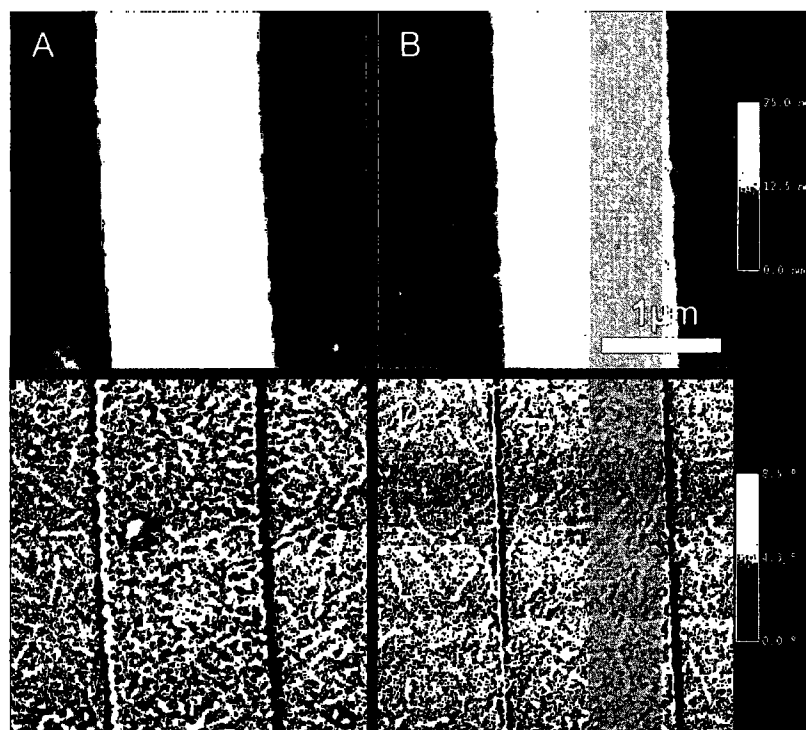


Figure 2.3 : AFM height and phase scans of Au (A,C) and Pt (B,D) electrodes. Very little differs between these two electrode materials, suggesting morphology is not an explanation for the variation in transport measurements.

Instead of morphological differences, we suggest that our observed deviations shown in figure 2.2 arise from charge transfer at the MO interface. This is consistent with previous work [20, 34, 37] which has suggested that a significant hole injection barrier exists in dedoped P3HT/Au systems. In this case, the HOMO level of the P3HT is not well aligned to the Fermi level of the gold electrode, presenting

only the deep tail states for injection. This may then lead to a depletion of charge carriers in the vicinity near the electrode. On the other hand, the Fermi level of Pt and Au/f-OPE would align well within the HOMO level of P3HT, thereby presenting a much lower barrier to injection, coupled with charge transfer (effectively doping the area near the electrode) and Fermi level pinning. This would help explain the reduction of device resistance in the Pt and Au/f-OPE case while device resistance is higher in the Au case.

Experimentally, we have evidence to support this hypothesis. Traditional semiconductor characterization is done using I_D - V_G transfer curves, but the large hysteresis found in measuring I_D - V_G curves makes it difficult to analyze the results. Instead we used I_D - V_{SD} curves which show several qualitative differences between Au and Pt devices, as shown in figure 2.4. Both devices have a channel length of 144nm and identical widths in order to remove any channel length effect on the electrical measurements. Comparing the left and right curves, the Pt electrodes (left) exhibit nearly an order of magnitude more current over the same V_G and V_{SD} range. Additionally, the Pt electrodes show a significant current even at $V_G = 0$. This again supports the idea that, in the area near the Pt electrodes, a large population of donated charge carriers exists whereas the opposite occurs in the Au case. Both an increase in device current and doped behavior make it seem that the Pt electrodes are transferring significant amounts of free carriers.

For additional evidence of charge transfer at the MO interface, we investigate the nature of the ZGB effect as a function of channel length. We chose a fixed $V_{SD} = -500\text{mV}$ for the data shown in figure 2.5(a). Initially, at the $5\mu\text{m}$ length, the ZGB currents for all three electrodes (Au, Au/f-OPE, Pt) are nearly identical. As the channel length decreases, the Pt electrode ZGB current increases by several

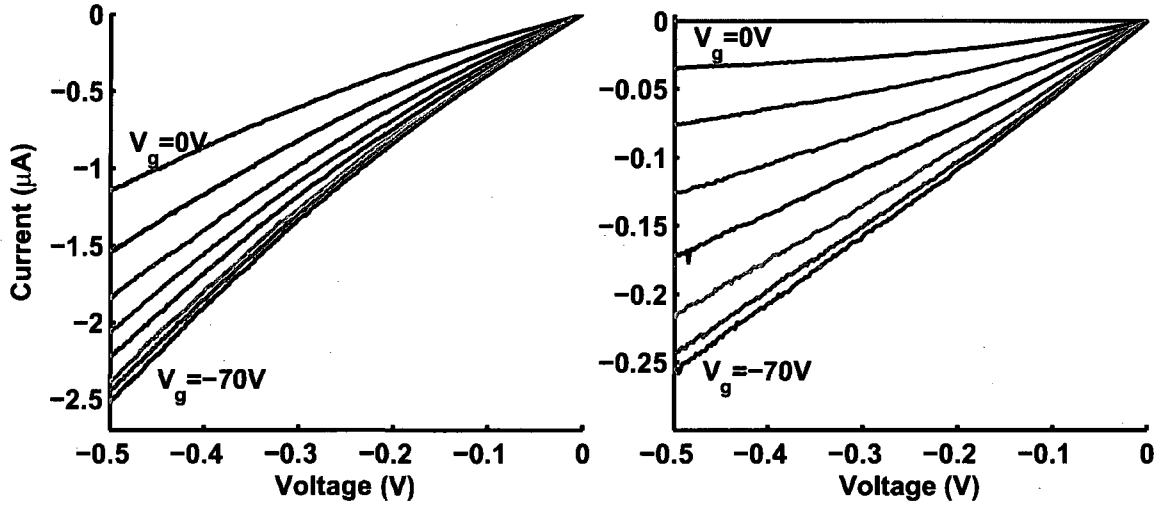
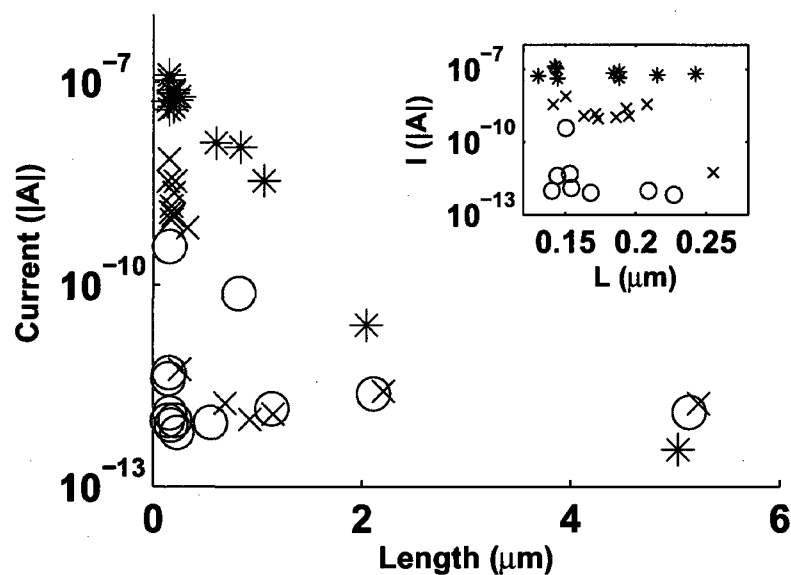
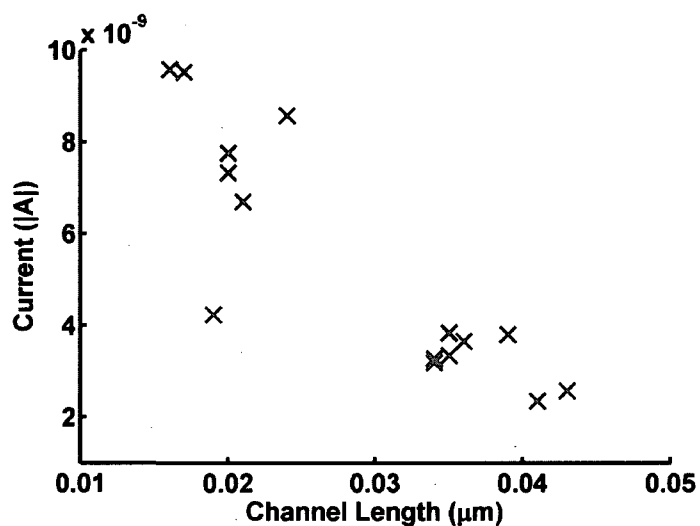


Figure 2.4 : I_D - V_{SD} curves for various V_G . Pt at left, Au at right. Note the order of magnitude difference between the Pt and Au currents, as well as the non-zero two terminal conduction in the Pt case. Channel length is 144nm, channel width is $50\mu\text{m}$, $T = 300\text{K}$ for both devices. As the channel length increases, the ZGB differences diminish.

orders of magnitude while the Au electrode current does not follow this trend. Note the intermediacy of the Au/f-OPE electrodes in the figure. They follow a similar trend as the Au electrodes until the channel length reaches 250nm, when the ZGB current suddenly increases by orders of magnitude. As the work function of the contact increases, there appears to be a marked increase in the magnitude of the ZGB current as well as change in its onset - the beginning of the ZGB current occurs at longer channel lengths with increased work functions. Again, this is consistent with our view that an area near the Pt (Au) electrode is effectively doped (depleted), and as these areas overlap, we begin to see the effects of this charge transfer. Since all electrode/OSC structures were prepared under identical processes, environmental doping or processing differences cannot be invoked to explain the $V_G = 0$ versus L conduction.



(a)



(b)

Figure 2.5 : (a) $V_G = 0$, two-terminal current (ZGB) versus channel length for Au, Au/f-OPE and Pt devices (legend in figure 2.2). The ZGB current is nearly identical for the $5\mu\text{m}$ channel but rapidly diverges as the channel lengths decrease, with Pt electrodes showing a strong increase in current. Inset: detail of current measured in the shortest channels. (b) Pt devices fabricated using the method in [1]. ZGB data collected at $V_{SD} = -500\text{mV}$.

Further evidence for charge transfer in Pt films was sought using ACSTM, presented earlier in chapter 1. For this particular experiment, a loop antenna geometry was used [38]. Care was used during the scan of both the Au- and Pt-P3HT films in order to ensure nearly identical scanning environments*. Both the ACSTM C-V measurement and the STM topography were acquired simultaneously, allowing for a direct comparison of topography and charge carrier concentrations. All scans were taken in ultrahigh vacuum with base pressure of 10^{-10} torr using a RHK STM and mechanically cut Pt:Rh (80:20) tips, with the gap resistance kept at a constant $100\text{G}\Omega$ to remove the influence of tip height. As previously mentioned, the samples used for ACSTM were prepared identically to those used in the electrical transport measurements, save for the addition of any SAMs.

Figure 2.6 shows both the topographical and ACSTM images acquired from the P3HT on Pt and Au[†]. The ACSTM data is not meant to be quantitative, but rather is used to show relative differences between the P3HT on Pt and Au. However, the color scale is directly proportional to the dC/dV data and, therefore, a representation of charge carrier concentration - similar to what is performed for Si devices [39]. Directly comparing the Pt and Au ACSTM data shows a marked contrast. Averaged over the entire image, the Pt ACSTM data shows a 25% increase in carrier concentration over the corresponding Au film. This trend repeats itself over several areas on each film. There exists higher spatial variation in the ACSTM signal on the Pt films, consistent

*Frequencies used were 300 and 300.004 MHz, approximately 3.7 dbm for the Pt sample and 3.0 dbm for the Au sample. The difference is due to the change in antenna position when switching between samples, and was adjusted by monitoring the input at the lock-in amplifier to ensure that the initial out-of-tunneling input signal strength at the difference frequency was the same for both samples. The same tip was used for both samples.

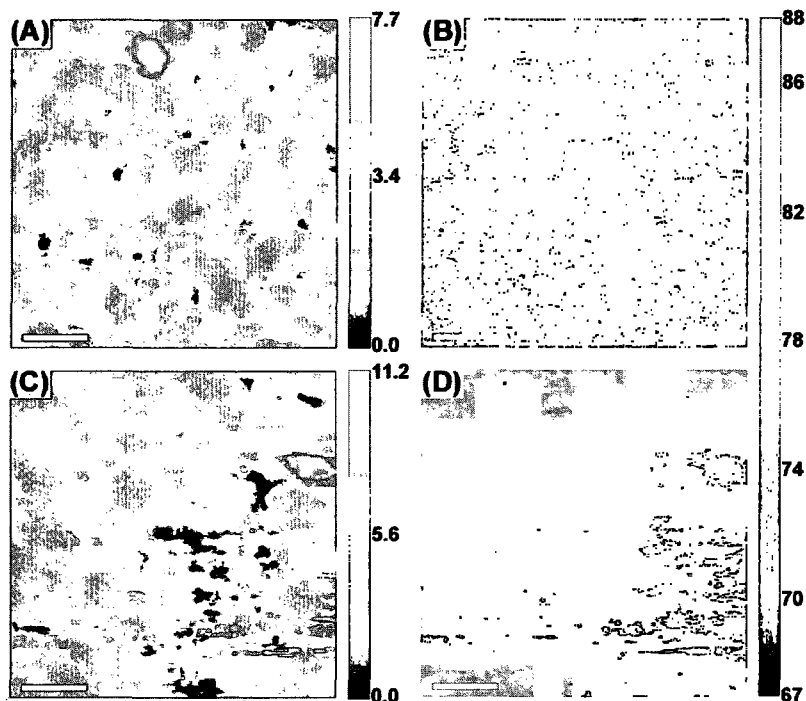


Figure 2.6 : Topography (A,C) and ACSTM (B,D) of Au (A,B) and Pt(C,D) films with P3HT deposited on top. All images were acquired at -1.0V sample bias, 10pA tunneling current and are $473\text{nm}\times 473\text{nm}$. The scale bars in all images are 94.6nm . The color bars are in units of nm for the topography images and in mV for the ACSTM images. The greater magnitude in (D) indicates a greater population of holes than in (B).

with the interpretation that the holes are more mobile near the Pt/OSC interface. As the tip bias is increased to -2V , the difference between the P3HT on Pt and on Au films increases, with the average carrier concentration going to 69% . While there is no direct comparison to the transistor structures used to perform the electrical measurements, clearly P3HT on Pt has a higher carrier concentration than P3HT on Au.

The topography images shown in figure 2.6 are fairly similar, and do not show

[†]Topography images were processed using plane-/offset-subtraction and median filtering in MATLAB, while ACSTM images were only median filtered.

any features that indicate correlation with the structure of the metal film below. In addition, the topography does not correlate well with the ACSTM data, indicating that the structure of the P3HT on the films does not determine the measured carrier concentration.

Our ACSTM and electronic transport measurements are consistent with the simple model developed by Paasch and Scheinert [40]. In their model, they describe the charge transfer and band bending associated with thin OSC films on metal substrates, which is precisely the situation presented in the ACSTM data. Additionally, at $V_G = 0$, this model should correlate well to transport immediately near the electrodes in our FET devices.

Assuming an exponential density of states in the organic (essentially the tail end of the Gaussian DOS) characterized by an energy width of $k_B T_0 = 0.1\text{eV}$, the local potential $U(x)$ in the organic semiconductor of thickness d as a function of the distance x away from the MO interface is given by

$$U(x) = U_d \pm k_B T_0 \ln \left[1 + \tan^2 \left(\frac{d-x}{2L_d} \exp \frac{|U_d|}{2k_B T_0} \right) \right] \quad (2.1)$$

where U_d is the potential at $x = d$, $L_d = \sqrt{\epsilon_p \epsilon_0 k_B T / 2e^2 n_i}$ is the intrinsic screening length, and $n_i = \sqrt{N_c N_v} \exp(-E_g / 2k_B T_0)$ is the effective intrinsic carrier density [40]. Here ϵ_p is the dielectric constant of the semiconductor, E_g is the band gap of the semiconductor, and N_c and N_v are the effective densities of states in the conduction and valence bands. The \pm sign is positive (negative) for hole (electron) accumulation.

The equation for the layer thickness d is given by

$$d = 2L_d \exp \left(\frac{-|V_d|}{2k_B T_0} \right) \arctan \sqrt{\exp \left(\frac{|V_s - V_d|}{k_B T_0} \right) - 1} \quad (2.2)$$

Here, $U_s = E_g/2 - \Phi_h$, where Φ_h is the hole injection barrier. Rough values used for our calculations are $N_c = N_v = 10^{21} \text{cm}^{-3}$, $E_g = 2\text{eV}$, $\epsilon_p = 3.24$ and $T = 300\text{K}$.

Using equations 2.1 and 2.2, we can determine the charge density, ρ in the OSC by solving Poisson's equation,

$$\epsilon\epsilon_0 \frac{d^2U}{dx^2} = -\rho. \quad (2.3)$$

We used numbers suitable for both Pt and Au in our calculations from photoemission experiments [34] and recent values of polaron formation energy [25]; these numbers manifest themselves as changes in the hole injection barrier in our calculations. For Pt, we used $\Phi_h = 0.6\text{eV}$, giving a carrier density of $9.6 \times 10^{17} \text{cm}^{-3}$; for gold, we used $\Phi_h = 1.2\text{eV}$, giving a carrier density of -10^{18}cm^{-3} with the minus sign indicating a depletion of hole density. While the quantitative nature of these results depends greatly on a detailed knowledge of the surface in question and the energetic structure of the P3HT, the qualitative trends shown here should be robust. This helps further buttress the claim that higher work function materials effectively dope a short region around the metal contact.

2.5 Conclusions

In this chapter, we showed that high work function metals (likely equal to or greater than the polaron formation energy) effectively dope the immediate vicinity of the metal/organic interface via charge transfer, leading to Fermi level pinning. For substrates with work functions lower than this, an opposite effect occurs with an effective depletion region near the contact. We showed through electronic transport measurements the marked difference between Pt and Au electrodes, notably in their respective device resistances and ZGB current. The ZGB current measurements are particularly interesting as the Au, Au/f-OPE and Pt data all converge at large channel lengths but rapidly diverge as the channel lengths shrink. We feel this indicates a large density of mobile charge carriers are transferred from Pt to the OSC. ACSTM measurements

further support this view by showing a large increase in charge carrier concentration in P3HT on Pt versus P3HT on Au.

Chapter 3

Final Remarks and Future Direction

In this thesis, we investigated the nature of charge transfer as a function of electrode work function. While previous research had used photoemission to indirectly probe the metal-organic semiconductor interface, we were able to directly observe charge transfer at the MO interface. We were able to show significant increases in source-drain current for high work function metals as the channel lengths decreased below $5\mu\text{m}$. Additionally, we showed that these same high work function metals effectively doped the area around the MO interface with mobile charge carriers leading to an order of magnitude more conduction at $V_G = 0$ than metals with lower work functions. As further support for this idea, ACSTM measurements performed on identically prepared Au and Pt films show an increase in the concentration of mobile carriers in P3HT on Pt films as compared to P3HT on Au films. We believe this shows, via electrical transport, that high work function materials do indeed transfer charge as the Fermi level is pinned.

We feel these experiments naturally lead to testing other organic semiconductors, such as pentacene. In particular, pentacene grows into large ordered domains, so while investigating the nature of charge transfer it may also be possible to investigate transport through ordered crystal domains on the nanometer scale. Additionally, we would like to use ultrafast terahertz time-domain spectroscopy to give us information about the nature of charge transfer at the nanometer scale. With a temporal resolution of tens of femtoseconds, it may be possible to observe charge carrier dynamics

with a high degree of precision.

Organic electronic materials are starting to become ubiquitous, and with the advent of smaller, cheaper and lower power consumer electronic devices, the need for a deep and thorough understanding of the behavior of metals and OSCs is paramount. We hope that this research is found useful in continuing innovation in this important field.

Bibliography

- [1] Fursina, A., Lee, S., Sofin, R. G. S., Shvets, I. V. & Natelson, D. Nanogaps with very large aspect ratios for electrical measurements. *Appl. Phys. Lett.* **92**, 113102 (2008).
- [2] Flexible, full-color OLED display (2007). URL <http://www.pinktentacle.com/2007/05/flexible-full-color-organic-el-display/>.
- [3] Britting, W. (ed.) *Physics of Organic Semiconductors* (Wiley-VCH, 2005).
- [4] Sun, S.-S. & Dalton, L. R. (eds.) *Introduction to Organic Electronic and Optoelectronic Materials and Devices* (CRC Press, 2008).
- [5] What to Do if Your Cover Is Not Flashing (2008). URL <http://www.esquire.com/features/cover-not-flashing-1008>.
- [6] Sze, S. M. & Ng, K. K. *Physics of Semiconductor Devices* (Wiley-Interscience, 2007), 3rd edn.
- [7] Podzorov, V. *et al.* Intrinsic Charge Transport on the Surface of Organic Semiconductors. *Phys. Rev. Lett.* **93**, 086602 (2004).
- [8] Sirringhaus, H. *et al.* Two-dimensional charge transport in self-organized, high-mobility conjugated polymers. *Nature* **401**, 685–688 (1999).
- [9] Bao, Z., Dodabalapur, A. & Lovinger, A. J. Soluble and processable regioregular

- poly(3-hexylthiophene) for thin film field-effect transistor applications with high mobility. *Appl. Phys. Lett.* **69**, 4108–4110 (1996).
- [10] McCullough, R. D., Lowe, R. D., Jayaraman, M. & Anderson, D. L. Design, synthesis, and control of conducting polymer architectures: structurally homogeneous poly(3-alkylthiophenes). *J. Org. Chem.* **58**, 904–912 (1993).
- [11] Anthony, J. E., Brooks, J. S., Eaton, D. L. & Parkin, S. R. Functionalized Pentacene: Improved Electronic Properties from Control of Solid-State Order. *J. Am. Chem. Soc.* **123**, 9482–9483 (2001).
- [12] Allen, C. F. H. & Gilman, L. A Synthesis of Rubrene. *J. Am. Chem. Soc.* **58**, 937–940 (1936).
- [13] Warta, W. & Karl, N. Hot holes in naphthalene: High, electric-field-dependent mobilities. *Phys. Rev. B* **32**, 1172–1182 (1985).
- [14] Hamadani, B. H. & Natelson, D. Temperature-dependent contact resistances in high-quality polymer field-effect transistors. *Appl. Phys. Lett.* **84**, 443–445 (2004).
- [15] Hamadani, B. H. & Natelson, D. Nonlinear charge injection in organic field-effect transistors. *J. Appl. Phys.* **97**, 064508 (2005).
- [16] Hamadani, B. H. & Natelson, D. Gated nonlinear transport in organic polymer field effect transistors. *J. Appl. Phys.* **95**, 1227–1232 (2004).
- [17] Koch, N. Energy levels at interfaces between metals and conjugated organic molecules. *J. Phys.: Condens. Matter* **20**, 184008 (2008).

- [18] Campbell, I. H. *et al.* Controlling Schottky energy barriers in organic electronic devices using self-assembled monolayers. *Phys. Rev. B* **54**, R14321–R14324 (1996).
- [19] Nesch, F., Rotzinger, F., Si-Ahmed, L. & Zuppiroli, L. Chemical potential shifts at organic device electrodes induced by grafted monolayers. *Chem. Phys. Lett.* **288**, 861 – 867 (1998).
- [20] Hamadani, B. H., Corley, D. A., Ciszek, J. W., Tour, J. M. & Natelson, D. Controlling Charge Injection in Organic Field-Effect Transistors Using Self-Assembled Monolayers. *Nano Lett.* **6**, 1303–1306 (2006).
- [21] Ishii, H. & Seki, K. Energy level alignment at organic/metal interfaces studied by uv photoemission: breakdown of traditional assumption of a common vacuum level at the interface. *Electron Devices, IEEE Transactions on* **44**, 1295–1301 (1997).
- [22] Hill, I. G., Rajagopal, A., Kahn, A. & Hu, Y. Molecular level alignment at organic semiconductor-metal interfaces. *Appl. Phys. Lett.* **73**, 662–664 (1998).
- [23] Scott, J. C. Metal-organic interface and charge injection in organic electronic devices. *J. Vac. Sci. & Tech. A* **21**, 521–531 (2003).
- [24] Rajagopal, A., Wu, C. I. & Kahn, A. Energy level offset at organic semiconductor heterojunctions. *J. Appl. Phys.* **83**, 2649–2655 (1998).
- [25] Tengstedt, C. *et al.* Fermi-level pinning at conjugated polymer interfaces. *Appl. Phys. Lett.* **88**, 053502 (2006).

- [26] Crispin, A., Crispin, X., Fahlman, M., Berggren, M. & Salaneck, W. R. Transition between energy level alignment regimes at a low band gap polymer-electrode interfaces. *Appl. Phys. Lett.* **89**, 213503 (2006).
- [27] Koch, N. & Vollmer, A. Electrode-molecular semiconductor contacts: Work-function-dependent hole injection barriers versus Fermi-level pinning. *Appl. Phys. Lett.* **89**, 162107 (2006).
- [28] Silveira, W. R. & Marohn, J. A. Microscopic View of Charge Injection in an Organic Semiconductor. *Phys. Rev. Lett.* **93**, 116104 (2004).
- [29] Ng, T. N., Silveira, W. R. & Marohn, J. A. Dependence of Charge Injection on Temperature, Electric Field, and Energetic Disorder in an Organic Semiconductor. *Phys. Rev. Lett.* **98**, 066101 (2007).
- [30] Bourgoin, J.-P., Johnson, M. B. & Michel, B. Semiconductor characterization with the scanning surface harmonic microscope. *Appl. Phys. Lett.* **65**, 2045–2047 (1994).
- [31] Schmidt, J., Rapoport, D. H. & Frohlich, H.-J. Microwave-frequency alternating current scanning tunneling microscopy by difference frequency detection: Atomic resolution imaging on graphite. *Rev. Sci. Instrum.* **70**, 3377–3380 (1999).
- [32] Vázquez, H., Dappe, Y. J., Ortega, J. & Flores, F. Energy level alignment at metal/organic semiconductor interfaces: “Pillow” effect, induced density of interface states, and charge neutrality level. *J. Chem. Phys.* **126**, 144703 (2007).
- [33] Vázquez, H. *et al.* Barrier formation at metal-organic interfaces: dipole formation and the charge neutrality level. *Appl. Surf. Sci.* **234**, 107 – 112 (2004).

- [34] Hamadani, B. H., Ding, H., Gao, Y. & Natelson, D. Doping-dependent charge injection and band alignment in organic field-effect transistors. *Phys. Rev. B* **72**, 235302 (2005).
- [35] Gundlach, D. J. *et al.* Contact-induced crystallinity for high-performance soluble acene-based transistors and circuits. *Nat. Mater.* **7**, 216–221 (2008).
- [36] Cai, L., Yao, Y., Yang, J., Price, D. W. & Tour, J. M. Chemical and Potential-Assisted Assembly of Thiolacetyl-Terminated Oligo(phenylene ethynylene)s on Gold Surfaces. *Chem. Mater.* **14**, 2905–2909 (2002).
- [37] Rep, D. B. A., Morpurgo, A. F. & Klapwijk, T. M. Doping-dependent charge injection into regioregular poly(3-hexylthiophene). *Org. Elec.* **4**, 201 – 207 (2003).
- [38] Lee, J., Tu, X. & Ho, W. Spectroscopy and Microscopy of Spin-Sensitive Rectification Current Induced by Microwave Radiation. *Nano Lett.* **5**, 2613–2617 (2005).
- [39] Donhauser, Z. J., McCarty, G. S. & Bumm, L. A. Weiss P. S. High resolution dopant profiling using a tunable AC scanning tunneling microscope. In Seiler, D. G. & et al. (eds.) *Characterization and Metrology for ULSI Technology: 2000 International Conference*, 641–646 (American Institute of Physics: New York, 2001).
- [40] Paasch, G. & Scheinert, S. Space charge layers in organic field-effect transistors with gaussian or exponential semiconductor density of states. *J. Appl. Phys.* **101**, 024514 (2007).